ChemSusChem

Research Article
doi.org/10.1002/cssc.202500812

Chemistry Europe
European Chemical Societies Publishing

www.chemsuschem.org

Spin State Differentiated [3Fe–4S] Cluster Electrocatalyzes Water Oxidation Efficiently

Rong Yan, Qian-Cheng Luo, Zi-Han Li, Na-Na Sun, Wei-Peng Chen, Yuan-Qi Zhai, Ho Johnny Chung Yin, Xiaotai Wang,* Xin Tu,* and Yan-Zhen Zheng*

Though there are many synthetic iron–sulfur clusters that have been reported to show catalytic activity mimicking the natural cofactors in metalloenzymes, the influence of the spin state on the catalytic property is seldom touched. Here, a disulfide-bridged triiron(II) complex is shown, namely $[Fe_3(Sip)_4][CF_3SO_3]_2$ (**$Fe_3(Sip)_4$**, HSip = sulfanylpropyliminomethyl-pyridine), can efficiently electrocatalyze water oxidation with a turnover frequency of 932 s^{-1} and Faraday efficiency of 86%, better than many iron-based catalysts. More importantly, the terminal low-spin ($S = 0$) iron(II) sites possessing a N4S2 first coordination environment, along with the synergetic catalysis of ligands, play a crucial role in the catalytic process. This research highlights the unconventional applications of iron–sulfur clusters in electrocatalytic water oxidation and underlines a promising avenue for developing innovative catalysts.

1. Introduction

Iron–sulfur clusters are pivotal cofactors in metalloenzymes, playing crucial roles in a wide array of biological processes, including photosynthesis, electron transfer, catalysis, substrate binding and activation, and nitrogen fixation.[1] These naturally occurring Fe–S clusters are typically categorized into three structural types based on the number of metal cores: rhombic $[Fe_2S_2]$, linear or cubic $[Fe_3S_4]$, and cubic $[Fe_4S_4]$ clusters.[1c] While di- and tetra-nuclear clusters were successfully synthesized, the linear trinuclear structure remained elusive for some time.[1,2] It was not until 1982 that Hagon and Holm et al. synthesized the first $[Fe_3S_4]$ cluster, which was identified as an isomer of the natural structure (**Figure 1**a), making a significant advancement.[2] Despite this, artificial linear $[Fe_3S_4]$ clusters remain scarce compared to other types due to its synthetic challenges.[2,3] One of the reasons is that the usually used thiolic ligands tend to form polymeric species during the reaction.[3c] To avoid the polymerization, tridentate mixed-donor ligands containing both nitrogen and sulfur atoms have been employed, which show much enhanced yields for constructing linear trinuclear species.[3c,3e]

On the other hand, synthetic iron–sulfur clusters demonstrate superior catalytic capabilities, such as hydrogen evolution[4] and carbon dioxide reduction.[5] However, due to the low-valent iron and electron-donating nature of sulfides (Table S1, Supporting Information), most reactions are reductive in nature. Water oxidation, a process requiring multiple electron transfers and high redox potential, is typically catalyzed by precious metal-based catalysts due to their superior activity and stability.[6] Not until 2014, Meyer et al. introduced the first iron-based molecular electrocatalyst for water oxidation reaction, achieving a turnover number (TON) of 29 by using a propylene carbonate/water mixed solution.[7] A breakthrough occurred in 2016 when Masaoka et al. reported a pentanuclear Fe complex[8] that exhibited a remarkable turnover frequency (TOF) of 1900 s^{-1} and TON of $\approx 10^6$–10^7 during a 120-minute electrolysis process in a mixed $MeCN/H_2O$ solution, setting a paradigm for iron-based electrocatalytic water oxidation.[9] Beyond that, there are only a dozen examples of electrochemically driven iron-based molecular catalysts, and the synergetic effect from ligands has been less explored in this field.[10]

In light of these considerations, we designed a trinuclear [3Fe-4S] cluster with a disparate coordination environment. The in situ formed sulfanylpropyliminomethyl-pyridine (HSip)

R. Yan, Q.-C. Luo, Z.-H. Li, N.-N. Sun, W.-P. Chen, Y.-Q. Zhai, Y.-Z. Zheng
Frontier Institute of Science and Technology
Interdisciplinary Research Center of Frontier Science and Technology
State Key Laboratory of Electrical Insulation and Power Equipment
MOE Key Laboratory for Nonequilibrium Synthesis and Modulation of Condensed Matter
Xi'an Key Laboratory of Electronic Devices and Material Chemistry
Xi'an Key Laboratory of Sustainable Energy and Materials Chemistry
Xi'an Jiaotong University
Xi'an, Shaanxi Province 710054, P. R. China
E-mail: zheng.yanzhen@xjtu.edu.cn

R. Yan, H. Johnny Chung Yin
Department of Materials Science and Engineering
City University of Hong Kong
83 Tat Chee Avenue, Kowloon 999077, Hong Kong

R. Yan, H. Johnny Chung Yin
Shenzhen Research Institute
City University of Hong Kong
Shenzhen 518057, P. R. China

X. Wang
Department of Chemistry and Materials Science
Xi'an Jiaotong-Liverpool University
Suzhou 215123, P. R. China
E-mail: Xiaotai.Wang@xjtlu.edu.cn

X. Tu
Department of Electrical Engineering and Electronics
University of Liverpool
Liverpool L69 3GJ, UK
E-mail: Xin.Tu@liverpool.ac.uk

Supporting information for this article is available on the WWW under https://doi.org/10.1002/cssc.202500812

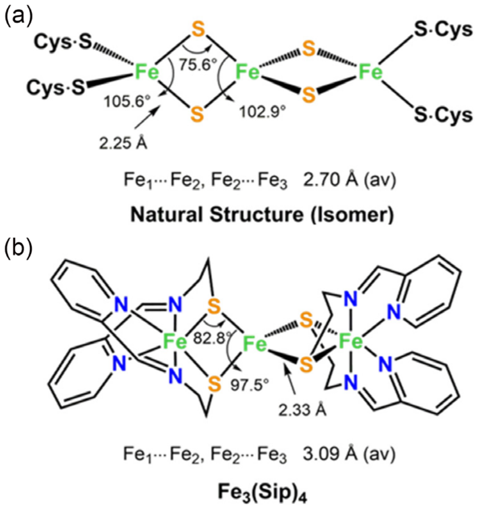

Figure 1. Geometries of a) The linear Fe_3S_4 cluster isomer in aconitase. b) An analog complex **$Fe_3(Sip)_4$** synthesized in this work ($Fe_{terminal}{-}N_{amine}$ 1.914(5) Å, $Fe_{terminal}{-}N_{pyridine}$ 1.982(5) Å, $Fe_{terminal}{-}S$ 2.336(18) Å, and $Fe_{middle}{-}S$ 2.330(19) Å).

ligand in complex $[Fe_3(Sip)_4][CF_3SO_3]_2$ **$Fe_3(Sip)_4$** successfully gives two identical terminal iron(II) centers with the first coordination sphere of N4S2, while the middle iron(II) center is four-coordinated with S4 surroundings. Magnetic and Mössbauer spectroscopy reveal that two terminal octahedral Fe(II) ions have a low-spin ($S = 0$) state, and the central one is in a high-spin ($S = 2$) state.[1c,3e] More importantly, **$Fe_3(Sip)_4$** exhibits superior catalytic activities for electrocatalyzing water oxidation, achieving a TOF of 932 s^{-1}, higher than many other iron-based catalysts. Property comparisons and density functional theory (DFT) studies revealed that the catalytic activity is mainly governed by the low-spin iron(II) centers as well as the reversible deprotonation/protonation of the coordinating pyridine nitrogen atoms. As such, this finding shows the unaware insights of spin states during the electrocatalyzing process and may provide additional new design criteria for next-generation catalysts.

2. Results and Discussion

Benefiting from the in situ Schiff base formation reaction of 2-aminoethanethiol and 2-pyridinecarboxaldehyde, **$Fe_3(Sip)_4$** was successfully prepared under solvothermal conditions. The complex was formed to block polymerization reactions involving thiolic ligands by employing tridentate mixed-donor ligands containing thiolate nitrogen–nitrogen–sulfur to provide necessary coordination sites on central Fe(II). Furthermore, using $Fe(OTf)_2$ as the initial iron source, combined with the sterically less hindered Sip ligand, successfully constructs a linear trinuclear complex **$Fe_3(Sip)_4$**. The complexation reactions between the Schiff base ligands and a stoichiometric amount of iron salt were performed in methanol without the base being added to deprotonate the thiol or benzenethiol. High-quality dark-colored crystals were collected.

Single-crystal X-ray diffraction determination manifests that **$Fe_3(Sip)_4$** crystallizes in the monoclinic space group *C*2/*c* (Table S2, Supporting Information). As shown in Figure 1b, the cationic core can be viewed as constructed from two mononuclear $[Fe^{II}(Sip)_2]$ fragments, further connected by one four-coordinated Fe(II) ion (crystal structure of **$Fe_3(Sip)_4$** is shown in Figure S1a, Supporting Information). Each Fe(II) ion in $[Fe^{II}(Sip)_2]$ is hexacoordinated and completed by four N atoms and two S atoms from two deprotonated Sip^- ligands adopting 2.211 bridging modes (Harris notation[11]) (Figure S1b, Supporting Information). The central Fe atom exhibits a tetrahedral coordination geometry ligated by four S atoms, with an average Fe…Fe distance to the outer Fe atoms is 3.086 (5) Å. The Fe—N and Fe—S bond lengths span 1.909–1.985 Å and 2.327−2.338 Å, respectively, comparable to those of similar Fe(II) complexes reported (Table S3, Supporting Information).[3c,3e] However, the average Fe—S bond lengths of $[Fe_3S_4]$ core in **$Fe_3(Sip)_4$** are longer than those in the natural structure, resulting in longer Fe…Fe distances along with smaller Fe−S−Fe angles and smaller S−Fe−S angles (Table S4, Supporting Information). In addition, the $[Fe_3S_4]$ core in **$Fe_3(Sip)_4$** is in a relatively symmetrical coordination environment, with three iron ions in a straight line, while the $[Fe_3S_4]$ substructure in Ref 3e is relatively bent. The oxidation states for Fe(II) ions are verified by bond valence sum calculations (Table S5, Supporting Information).[12] Moreover, complex **$Fe_3(Sip)_4$** solids can be easily dissolved in CH_3CN under stirring (Figure S2, Supporting Information).

X-ray powder diffraction measurements of crystalline powder samples were conducted (Figure S3, Supporting Information), which shows that the prepared sample is phase pure. The chemical states of Fe were confirmed using X-ray photoelectron spectroscopy (XPS). As shown in the Fe 2*p* spectrum (**Figure 2**a), the peaks at binding energies at 708.5 eV and 722.0 eV were assigned to the Fe $2p_{3/2}$ and Fe $2p_{1/2}$, respectively. The relative intensities of these peaks and their satellite features confirm the existence of iron oxidation states (Fe^{II}), which is consistent with the previous evidence.[13]

For the verification of the accuracy of spin state identification, the powder zero-field ^{57}Fe Mössbauer spectroscopy of **$Fe_3(Sip)_4$** was conducted at 80 K (Figure 2b). It revealed two distinctive doublets, including two iron sites in a ≈2:1 ratio with $\delta = 0.33$ mm s^{-1}, $\Delta E_Q = 0.80$ mm s^{-1} (≈66.3%, red line) for the hexa-coordinate terminal Fe and $\delta = 0.73$ mm s^{-1}, $\Delta E_Q = 2.28$ mm s^{-1} (≈33.7%, green line) for the tetra-coordinate middle Fe. The smaller ΔE_Q is aligned with two low-spin, six-coordinate geometry Fe ions, while the larger one is assigned to the high-spin, four-coordinate configuration of Fe.[14] The spin states are similar to the reported structures.[3e]

The temperature dependence of the magnetic susceptibility for **$Fe_3(Sip)_4$** was measured on a polycrystalline sample under a 1000 Oe dc field within 2–300 K (Figure S4, Supporting Information). The $\chi_M T$ product of 3.36 cm^3 K mol^{-1} at room temperature approach to the theoretical value of 3.0 cm^3 mol^{-1} K for a single free Fe(II) ion in the high-spin state ($g = 2$, $S = 2$), indicative of two terminal Fe(II) ions in the low spin state. These results were also consistent with the Mössbauer data.

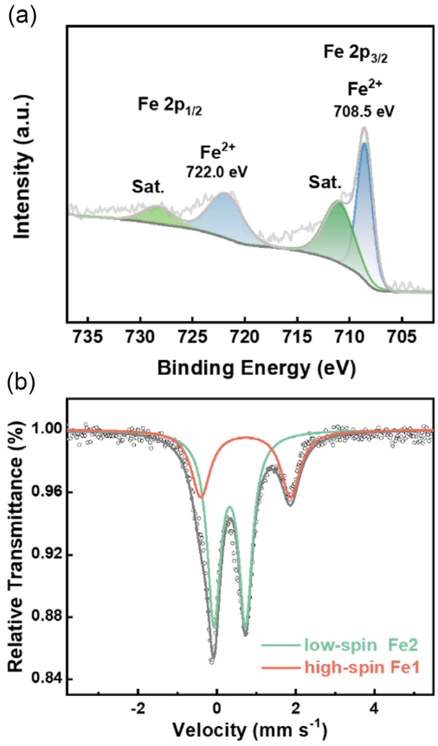

Figure 2. a) XPS spectra of Fe 2*p* for **Fe_3(Sip)$_4$**. b) The powder zero-field ^{57}Fe Mössbauer spectroscopy of **Fe_3(Sip)$_4$** at 80 K.

As shown in **Figure 3**a, cyclic voltammetry (CV) of **Fe_3(Sip)$_4$** in a 0.1 M Bu_4NPF_6 MeCN revealed three oxidation peaks at -0.40, 0.02, and 0.95 V versus ferrocenium/ferrocene (Fc/Fc^+), respectively. By comparing the CV potentials of $Fe(OTf)_2$ and ligand Sip, the peak at -0.40 V versus Fc/Fc^+ is assigned to redox of ligands, —C═N— bonds in imide, on account of one distinct feature about imine bonds is the reductive potential is generally from -0.40 to -0.90 V versus Fc/Fc^+ (Figure S5 and S6, Supporting Information).[15,16] In particular, the change of the imine bond here does not participate in the subsequent water oxidation reaction and does not affect the stability of the catalyst. The latter two peaks are attributed to the successive oxidation of three Fe(II) centers to Fe(III). The current amplitude for the reversible redox peak at 0.95 V versus Fc/Fc^+ is 2.74 times than that of the quasireversible redox peak at 0.02 V versus Fc/Fc^+, suggesting that the electrochemical reaction at high voltage is more likely a two-electron simultaneous oxidation process for the two hexacoordinated Fe(II) atoms in **Fe_3(Sip)$_4$** since they not only possess the same coordination environment but also can be oxidized independently (Figure 3a). According to the electrochemical theory, the current passed for the one-electron process (A) and two-electron process (B) is set as $n^{1/2}$ and $n^{3/2}$, respectively. When $n = 1$, the value for A equals 1. Likewise, B is 2.82 for $n = 2$.[16,17] Thus, the calculated B/A ratio of 2.82 is in good agreement with the above experimental result, 2.74, shown in Figure 3a. Upon the addition of H_2O, a rapid increase of the catalytic current can be observed (Figure S7, Supporting Information), indicating that **Fe_3(Sip)$_4$** has the potential for the catalysis of water oxidation. After adjusting the upper limit of the potential range, the redox peak current in MeCN/H_2O solutions increased to a certain extent compared to those in MeCN (Figure S8, Supporting Information). Because of the coordination of H_2O/OH^- with Fe, the electron density of the metal center increases, making it more prone to oxidation, and following the redox peak of the ligand shifts toward the negative potential direction. Notably, at 1.26 V versus Fc/Fc^+, a strong irreversible oxidation peak belonging to the $Fe^{III/IV}$ change was observed, which was consistent with the reported potential distribution of the Fe^{IV} peak, indicating the increase of valence states for the iron center during the water oxidation process as experimental evidence for the mechanism speculation.[10]

To further verify if there is any contribution from ligand or reactant, $Fe(OTf)_2$, Sip, 2-pyridinecarboxaldehyde, and 2-aminoethanethiol were also tested under the same conditions. As shown in Figure 3b, the activities of ligand Sip, 2-pyridinecarboxaldehyde, and 2-aminoethanethiol were negligible, and the raw iron salt $Fe(OTf)_2$ generates small catalytic currents, indicating that **Fe_3(Sip)$_4$** dominates the contribution to catalytic currents. This comparison further verifies that water oxidization is driven by the whole **Fe_3(Sip)$_4$** molecule, not depending on the individual ligands or some components.

The constant limiting currents were also observed in Figure S9, Supporting Information, when water concentration is higher than 5.6 mM, indicating that the substrate (H_2O) amount is sufficient to reach the purely kinetic condition. In the meantime, the impact of the catalyst dosage on the reaction was also explored, which found that the i_{cat} values had a linear relationship with [cat] when [cat] is in the range of 0.1–0.3 mM. This means that the rate law for O_2 evolution catalyzed by **Fe_3(Sip)$_4$** can be expressed by using a pseudo-first-order rate constant, k_{cat}, as $d[O_2]/dt = k_{cat}[cat]$ (Figure S10, Supporting Information). A linear correlation was observed between the reduction peak currents (i_p) and the square root of the scan rate ($v^{1/2}$), suggesting that these reduction waves were diffusion-controlled (Figure S11 and S12, Supporting Information). The TOF and TON for the H_2O-to-O_2 conversion were determined to be 932 s^{-1} and 1.68×10^6 (Figure 3c and S13, Table S6, Supporting Information), surpassing most iron-based molecular electrocatalysts (Table S7, Supporting Information).

To quantitatively detect the efficiency of the water oxidation reaction, the controlled potential electrolysis (CPE) was then operated on a two-compartment cell separated by an anion-exchange membrane using indium tin oxide (ITO) as the working electrode in a MeCN/H_2O solution containing 0.2 mM **Fe_3(Sip)$_4$** (Figure 3d). After electrolysis for 30 min, 0.35 mL of O_2 was collected from the sealed electrochemical anode cell and detected by gas chromatography, corresponding to Faradic efficiency 86% (Figure S14a, Supporting Information). The peak position at 11 min belongs to CO_2 and was not detected. H_2O_2 (≈8%) was detected as a byproduct of the anode reaction. A small amount of H_2 was detected from the cathode side (Figure S14b, Supporting Information).

A notable issue is whether the trinuclear complex might dissociate to a monomeric species in solution. We, thus, examined the high-resolution mass spectrometry (HR-MS). HR-MS displayed a prominent peak at $m/z = 413.9913$ for **Fe_3(Sip)$_4$**, corresponding

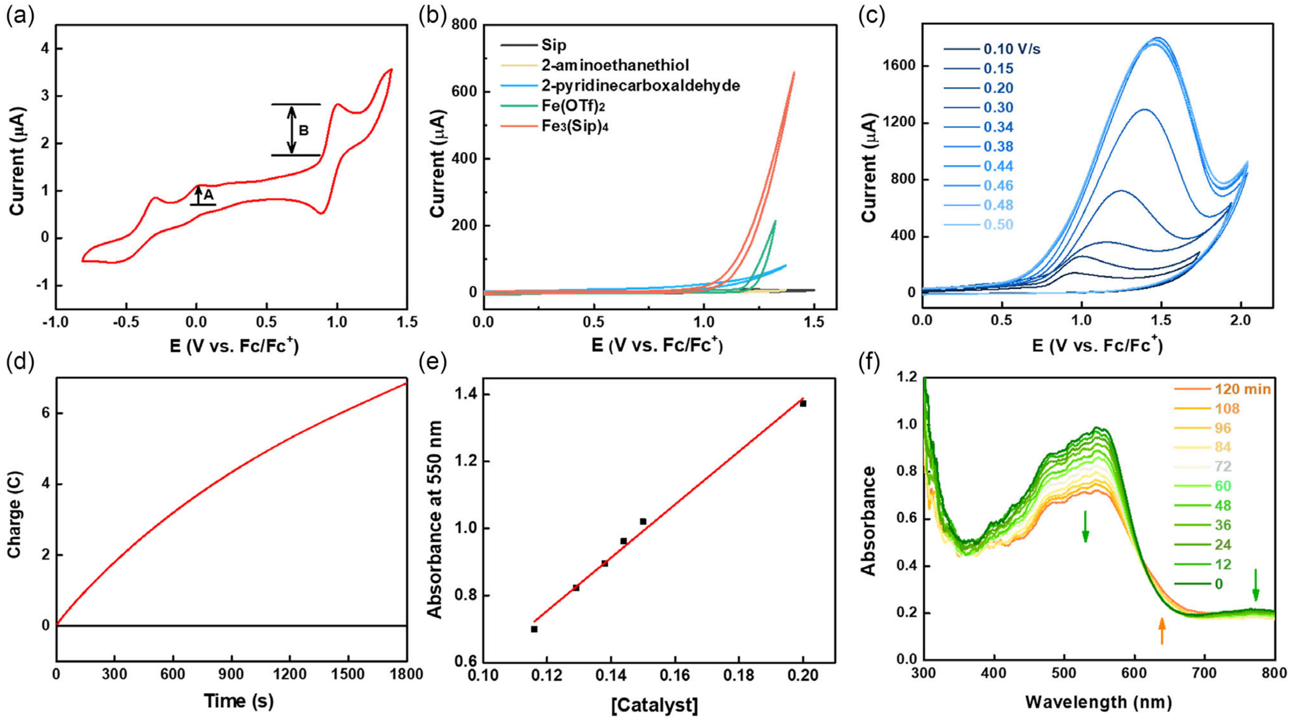

Figure 3. CV of **$Fe_3(Sip)_4$** (0.2 mM) in MeCN with Bu_4NPF_6 (0.1 M) a) at a scan rate of 10 mV s^{-1}. b) CVs of **$Fe_3(Sip)_4$**, Fe(OTf)$_2$, ligand Sip, and its two components in MeCN/H_2O. c) CVs of **$Fe_3(Sip)_4$** (0.2 mM) at different scan rates from 0.10 to 0.50 V s^{-1} in MeCN/H_2O (9:1) mixed solution (i_{cat}). d) CPE at 1.40 V versus Fc/Fc$^+$ with (red line) and without (black line) 0.2 mM **$Fe_3(Sip)_4$**. e) Plot of absorbances at 550 nm as a function of concentration of catalyst. f) The change of UV–vis absorption spectra during the water oxidation reaction of 0.2 mM **$Fe_3(Sip)_4$**.

to the reasonable formula of $Fe_3(Sip)_4]^{2+}$ (cal. 413.9991), respectively. Identifying that **$Fe_3(Sip)_4$** was integrated (Figure S15, Supporting Information). In addition, considering the formation of heterogeneous FeO_x species from aqueous Fe^{2+} or molecular precursors under catalytic conditions, we systematically evaluated the structural integrity of **$Fe_3(Sip)_4$** during electrocatalysis. The catalytic currents remained almost unchanged, and CV curves were basically identical and superimposable after 30 min of electrolysis (Figure S16, Supporting Information). After rinsing the ITO electrode, CV scans in a blank electrolyte exhibited negligible current (Figure S17, Supporting Information). The surface morphology of ITO electrodes pre- and post-electrolysis at 1.45 V versus Fc/Fc$^+$ was monitored by scanning electron microscopy (SEM) and energy-dispersive X-Ray spectroscopy (EDX). SEM showed that the ITO surface remained unchanged, and the precipitates of iron oxide were not observed during electrolysis (Figure S18, Supporting Information). EDX spectra revealed no Fe element deposited on the ITO surface after reaction (Figure S19, Supporting Information). The XPS analyses for the used ITO electrode indicated that no new heterogeneous phase (film or precipitation) existed on the surface of the electrode after electrolysis (Figure S20, Supporting Information). Resonance Raman spectra of the solutions pre- and postreaction reveal consistent peak profiles, suggesting that the structural integrity of the complex was preserved throughout the electrolysis process (Figure S21, Supporting Information). Meanwhile, the peak values of the UV–visible absorption spectrum for both the powder and solution samples are also close, further confirming that the **$Fe_3(Sip)_4$** structure remains unchanged in the solution (Figure S22, Supporting Information). All the above results show that **$Fe_3(Sip)_4$** exhibits stability during the catalytic process.

We also studied the electronic behaviors in MeCN in detail through UV–vis spectroscopy. **$Fe_3(Sip)_4$** displays bands at 550 nm, related to the d–d transitions (Figure S23, Supporting Information). Absorbance intensity was linearly dependent on the **$Fe_3(Sip)_4$** concentration from 0.116 to 0.20 mM (Figure 3e), indicating that the trinuclear complex remained intact in MeCN. In addition, CPE for **$Fe_3(Sip)_4$** generated the slow isosbestic conversion with a broad band from 470 to 600 nm, corresponding to a ligand-to-iron(III) charge-transfer transition (Figure 3f).[18] There is a slight change in the color of solutions before and after electrolysis for the gradual oxidation from Fe^{II} to Fe^{III}, consistent with the UV spectra (Figure S2, Supporting Information).

The influence of pH values of the electrolyte was examined. The results show that the initial pH of the solution was 5.5, and after half an hour of reaction, the pH was ≈5.4. The catalytic currents were also tested using buffer solutions at different pH values (Figure S24, Supporting Information). As the pH decreased, the current also gradually declined. When pH was below 4.8, the current decayed by more than half, regarded as acid tolerance.

To understand the catalytic process, the kinetic isotope effect (KIE) of the catalyst was evaluated by Equation (1). The ratio of the steady-state catalytic currents at the bias of 1.5 V (versus Fc/Fc^+) in pH 7.0 and pD 7.0 KPi solution (denoted as $i_{cat,H2O}$ and $i_{cat,D2O}$) was determined with a KIE value of 2.93 calculated according to Equation (1) and Figure S25, Supporting Information, which is larger than 2. Empirically, it possibly contains the water nuclear attack process.[19]

$$KIE = k_{\text{cat},H_2O}/k_{\text{cat},D_2O} = \left(i_{\text{cat},H_2O}/i_{\text{cat},D_2O}\right)^2 \quad (1)$$

To identify the true active site within the complex, we utilized the complex from ref 3e as a counterpart. The compounds in the literature have a highly similar valence and configuration to that of **$Fe_3(Sip)_4$**, along with the distribution of spin states. There are six-coordinated low-spin iron atoms on both sides with a central four-coordinated high-spin iron atom. Only the ligand is different, with no pyridine nitrogen coordination. Therefore, this complex would be a very suitable case for comparison. We synthesized and tested the catalytic activities of the complex. The results showed that after adding H_2O, the catalytic current was almost unchanged (Figure S26, Supporting Information). Thus, it was inert toward the water oxidation reaction. This test not only excluded the catalytic contribution of the central iron but also demonstrated the uniqueness of ligand design in **$Fe_3(Sip)_4$**.

A possible catalytic cycle is proposed based on the above evidence (**Figure 4**a). Regarding the highly similar coordination environments around both terminal iron centers, here, we merely investigate and discuss the reaction mechanism induced by one of the individual sites for simplification. Complex **$Fe_3(Sip)_4$** initially undergoes a two-step continuous oxidation process, generating a trinuclear Fe(III) iron cluster **S_0**, considered as the beginning of the catalytic cycle. Then, the attack of the water molecule squeezes out one of the coordinated pyridine nitrogen, keeping the Fe(III) site in the octacoordinated geometry. DFT calculations demonstrate that a proton transfer process exists from the water molecule to the distant pyridine ring, realizing the protonation of the ligand (**S_1**). The reactive energy of this water attack reaction is determined as -3.37 kcal mol^{-1}, together with its activation barrier of 11.57 kcal mol^{-1}. Then, a similar procedure occurs when the other pyridine nitrogen is far away and undergoes protonation, which is also exoergic with the energy change of -1.16 kcal mol^{-1} (**S_1** + $H_2O \rightarrow$ **S_2**) with an activation barrier of 7.59 kcal mol^{-1} (Figure S27, Supporting Information). To determine the presence of protonated pyridine in **S_1** and **S_2**, we also performed the Fourier transform infrared spectroscopy (FT-IR) measurements for the electrolyte solution at 1.13 V which exactly contains **S_1** and **S_2** species (Figure S28, Supporting Information), and the N–H characteristic stretching vibrational peak can be evidently observed at 2628 cm^{-1} experimentally. Also, this peak is exactly consistent with the DFT calculated vibrational energies of that at 2747 cm^{-1} (Mode 215) for **S_1** as well as 2537 and 2554 cm^{-1} (Mode 222 and 223) for **S_2** (GIF S1–S3). Then, a proton on coordinated hydroxyl is eliminated together with a single electron transfer, affording the intermediate

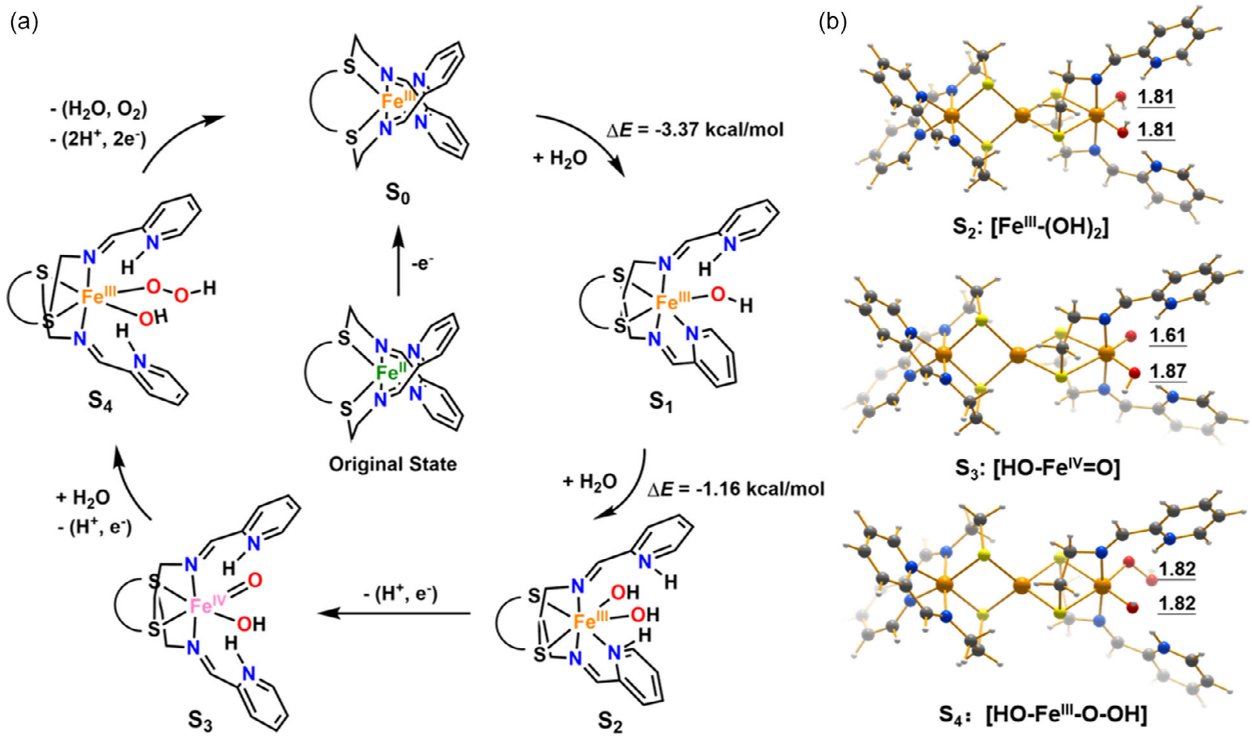

Figure 4. a) Proposed catalytic cycle for water oxidation catalyzed by **$Fe_3(Sip)_4$**. b) Structure and bond length (Å) of Fe—O for transition states S_2, S_3, and S_4 (Table S8, Supporting Information).

$\mathbf{S_3}$ with the formation of a Fe(IV) ion, while we can not deduce whether the proton-coupled electron transfer exists or not in this step based on the present experimental evidence. The distance of one of the Fe—O bonds in $\mathbf{S_3}$'s optimized structure is largely shortened from ≈1.81 Å to 1.61 Å, and the calculated spin populations on this Fe(IV) ion are around 1.43, which indicates it is at the intermediate spin state (Figure 4b, Table S9 and S10, Supporting Information). Later, the insertion of another water and the transformation of one proton and one electron occur, together with the decline of the valence of the Fe ion, leading to the formation of O—O bond in $\mathbf{S_4}$. DFT calculations show that the Fe—O bond length increases to around 1.82 Å, and the spin populations on the corresponding Fe center also reduce to 0.99, confirming the formation of trivalent iron (Figure 4b and Table S9 and S10, Supporting Information). Following a double electron oxidation process and two protons transferring to the environment, the gas O_2 releases rapidly, and the complex $\mathbf{S_4}$ transforms to $\mathbf{S_0}$, initiating a new catalytic cycle. In this catalytic process, the reversible ligand protonation demonstrates the presence of collaborative catalysis, which guarantees the high efficiency of water oxidation.[20,10b]

3. Conclusions

In summary, we have successfully isolated a rare trinuclear iron–sulfur cluster that largely mimics the natural enzyme cofactors. This cluster features two terminal low-spin and one central high-spin iron(II) centers linked by two disulfide bridges. The resulting compound exhibits superior catalytic performance in water oxidation, mainly attributed to low-spin iron sites with the exceptional N4S2 first coordination sphere as well as the reversible protonation of the pyridine nitrogen. As this synergetic effect from the pyridine ligand is less explored in the catalytic process, this research may provide a new paradigm to design next-generation electrocatalysts.

Acknowledgements

R.Y. and Q.-C.L. contributed equally to this work. This work was supported by the National Natural Science Foundation of China (No. 22375157), the Programme of Introducing Talents of Discipline to Universities (B23025), the Medical-Engineering Cross Project of the First Affiliated Hospital of XJTU (QYJC02), "Scientists + Engineers" Team Building Project of Qin Chuang Yuan (2022KXJ-088) and the assistance from the Instrument Analysis Centre of Xi'an Jiaotong University. X.W. acknowledges support from Xi'an Jiaotong-Liverpool University, the Suzhou Industrial Park High Quality Innovation Platform of Functional Molecular Materials and Devices (YZCXPT2023105), and the Xi'an Jiaotong-Liverpool University Advanced Materials Research Center (AMRC).

Conflict of Interest

The authors declare no competing interests.

Data Availability Statement

The data that support the findings of this study are available in the supplementary material of this article.

Keywords: artificial synthesis · electrocatalysis · iron–sulfur clusters · molecular catalysts · water oxidation

[1] a) A. E. Boncella, E. T. Sabo, R. M. Santore, J. Carter, J. Whalen, J. D. Hudspeth, C. N. Morrison, *Coordination Chem. Rev.* **2022**, *453*, 214229. b) H. Beinert, R. H. Holm, E. Münck, *Science* **1997**, *277*, 653. c) P. Venkateswara Rao, R. H. Holm, *Chem. Rev.* **2004**, *104*, 527. d) M. C. Kennedy, T. A. Kent, M. Emptage, H. Merkle, H. Beinert, E. Münck, *J. Biol. Chem.* **1984**, *259*, 14463.

[2] K. S. Hagen, R. H. Holm, *J. Am. Chem. Soc.* **1982**, *104*, 5496.

[3] a) K. S. Hagen, A. D. Watson, R. H. Holm, *J. Am. Chem. Soc.* **1983**, *105*, 3905. b) F. M. MacDonnell, K. Ruhlandt-Senge, J. J. Ellison, R. H. Holm, P. P. Power, *Inorg. Chem.* **1995**, *34*, 1815. c) M. Mikuriya, T. Kotera, F. Adachi, M. Handa, M. Koikawa, H. Okawa, *Bull. Chem. Soc. Jpn.*, **1995**, *68*, 574. d) S. C. Davies, M. C. Smith, D. L. Hughes, D. J. Evans, *Acta Crystallogr. E Struct. Rep. Online*, **2002**, *58*, m658. e) U. K. Das, S. L. Daifuku, S. I. Gorelsky, I. Korobkov, M. L. Neidig, J. J. Le Roy, M. Murugesu, R. T. Baker, *Inorg. Chem.* **2016**, *55*, 987.

[4] a) Y. Liu, C. Pulignani, S. Webb, S. J. Cobb, S. Rodríguez-Jiménez, D. Kim, R. D. Milton, E. Reisner, *Chem. Sci.* **2024**, *15*, 6088. b) W. P. Brezinski, M. Karayilan, K. E. Clary, N. G. Pavlopoulos, S. Li, L. Fu, K. Matyjaszewski, D. H. Evans, R. S. Glass, D. L. Lichtenberger, J. Pyun, *Angew. Chem. Int. Ed.* **2018**, *57*, 11898.

[5] V. Waser, M. Mukherjee, R. Tachibana, N. V. Igareta, T. R. Ward, *J. Am. Chem. Soc.* **2023**, *145*, 14823.

[6] a) A. M. Geer, C. Musgrave Iii, C. Webber, R. J. Nielsen, B. A. McKeown, C. Liu, P. P. M. Schleker, P. Jakes, X. Jia, D. A. Dickie, J. Granwehr, S. Zhang, C. W. Machan, W. A. Goddard, T. B. Gunnoe, *ACS Catal.* **2021**, *11*, 7223. b) N. Vereshchuk, M. Gil-Sepulcre, A. Ghaderian, J. Holub, C. Gimbert-Suriñach, A. Llobet, *Chem. Soc. Rev.* **2023**, *52*, 196.

[7] M. K. Coggins, M.-T. Zhang, A. K. Vannucci, C. J. Dares, T. J. Meyer, *J. Am. Chem. Soc.* **2014**, *136*, 5531.

[8] M. Okamura, M. Kondo, R. Kuga, Y. Kurashige, T. Yanai, S. Hayami, V. K. K. Praneeth, M. Yoshida, K. Yoneda, S. Kawata, S. Masaoka, *Nature* **2016**, *530*, 465.

[9] a) A. Cingolani, I. Gualandi, E. Scavetta, C. Cesari, S. Zacchini, D. Tonelli, V. Zanotti, P. Franchi, M. Lucarini, E. Sicilia, G. Mazzone, D. Nanni, R. Mazzoni, *Catal. Sci. Technol.* **2021**, *11*, 1407. b) K. G. Kottrup, S. D'Agostini, P. H. Van Langevelde, M. A. Siegler, D. G. H. Hetterscheid, *ACS Catal.* **2018**, *8*, 1052. c) V. K. K. Praneeth, M. Kondo, M. Okamura, T. Akai, H. Izu, S. Masaoka, *Chem. Sci.* **2019**, *10*, 4628.

[10] a) S. M. Al-Zuraiji, T. Benkó, L. Illés, M. Németh, K. Frey, A. Sulyok, J. S. Pap, *J. Catal.* **2020**, *381*, 615. b) H. Zhang, X. Su, F. Xie, R. Liao, M. Zhang, *Angew. Chem. Int. Ed.* **2021**, *60*, 12467. c) E. L. Demeter, S. L. Hilburg, N. R. Washburn, T. J. Collins, J. R. Kitchin, *J. Am. Chem. Soc.* **2014**, *136*, 5603.

[11] R. A. Coxall, S. G. Harris, D. K. Henderson, S. Parsons, P. A. Tasker, R. E. P. Winpenny, *J. Chem. Soc., Dalton Trans.* **2000**, *14*, 2349.

[12] H. Zhang, F. Xie, Y. Guo, Y. Xiao, M. Zhang, *Angew. Chem. Int. Ed.* **2023**, *62*, e202310775.

[13] A. Matamoros-Veloza, O. Cespedes, B. R. G. Johnson, T. M. Stawski, U. Terranova, N. H. De Leeuw, L. G. Benning, *Nat. Commun.* **2018**, *9*, 3125.

[14] C. Gallenkamp, U. I. Kramm, J. Proppe, V. Krewald, *Int. J. Quantum Chem.* **2021**, *121*, e26394.

[15] L. Wang, C. Xu, W. Zhang, Q. Zhang, M. Zhao, C. Zeng, Q. Jiang, C. Gu, Y. Ma, *J. Am. Chem. Soc.* **2022**, *144*, 8961.

[16] A. J. Bard, L. R. Faulkner, *Russ. J. Electrochem.* **2002**, *38*, 1364.

[17] L. D. Wickramasinghe, R. Zhou, R. Zong, P. Vo, K. J. Gagnon, R. P. Thummel, *J. Am. Chem. Soc.* **2015**, *137*, 13260.

[18] T. M. Pangia, C. G. Davies, J. R. Prendergast, J. B. Gordon, M. A. Siegler, G. N. L. Jameson, D. P. Goldberg, *J. Am. Chem. Soc.* **2018**, *140*, 4191.

[19] a) Y. Liu, Y. Han, Z. Zhang, W. Zhang, W. Lai, Y. Wang, R. Cao, *Chem. Sci.* **2019**, *10*, 2613. b) Z. Chen, J. J. Concepcion, X. Hu, W. Yang, P. G. Hoertz, T. J. Meyer, *Proc. Natl. Acad. Sci. U.S.A.* **2010**, *107*, 7225.

[20] a) R.-Z. Liao, S. Masaoka, P. E. M. Siegbahn, *ACS Catal.* **2018**, *8*, 11671. b) Y. Zhang, H. Zhang, A. Liu, C. Chen, W. Song, J. Zhao, *J. Am. Chem. Soc.* **2018**, *140*, 3264. c) L. Xie, X. Zhang, B. Zhao, P. Li, J. Qi, X. Guo, B. Wang, H. Lei, W. Zhang, U. Apfel, R. Cao, *Angew. Chem. Int. Ed.* **2021**, *60*, 7576.

Manuscript received: April 16, 2025
Revised manuscript received: July 9, 2025
Version of record online: